Cao *et al. Chem Synth* 2023;3:23
**DOI:** 10.20517/cs.2023.09

**Chemical Synthesis**

**Research Article**

**Open Access**

# High-throughput screening of B/N-doped graphene supported single-atom catalysts for nitrogen reduction reaction

**Ning Cao[1], Nan Zhang[2], Ke Wang[1], Keping Yan[1,3], Pengfei Xie[1,3,*]**

[1]College of Chemical and Biological Engineering, Zhejiang University, Hangzhou 310027, Zhejiang, China.
[2]State Key Laboratory of Coordination Chemistry, School of Chemistry and Chemical Engineering, Nanjing University, Nanjing 210008, Jiangsu, China.
[3]Shanxi-Zheda Institute of Advanced Materials and Chemical Engineering, Taiyuan 030032, Shanxi, China.

***Correspondence to:** Prof. Pengfei Xie, College of Chemical and Biological Engineering, Zhejiang University, 38 Zhe-da Road, Hangzhou 310027, Zhejiang, China. E-mail: pfxie@zju.edu.cn

**How to cite this article:** Cao N, Zhang N, Wang K, Yan K, Xie P. High-throughput screening of B/N-doped graphene supported single-atom catalysts for nitrogen reduction reaction. *Chem Synth* 2023;3:23. https://dx.doi.org/10.20517/cs.2023.09

**Received:** 19 Feb 2023 **First Decision:** 27 Mar 2023 **Revised:** 17 Apr 2023 **Accepted:** 25 Apr 2023 **Published:** 15 May 2023

**Academic Editors:** Bao-Lian Su, Da-Gang Yu , Yuefeng Liu **Copy Editor:** Dong-Li Li **Production Editor:** Dong-Li Li

## Abstract

Transitional metal single atom ($TM_1$) doped graphene catalysts have been widely applied in electrochemical $N_2$ reduction reaction (NRR). However, it remains a challenge for the rational design of highly active and selective electrocatalysts owing to limited knowledge of structure-activity correlations. Here, we adopted first-principle calculations to high-throughput screen the NRR performance of $TM_1$ coordinated with two boron and two nitrogen atoms in graphene ($TM_1$-$B_2N_2$/G). A "five-step" strategy was implemented by progressively considering different metrics such as stability, $N_2$ adsorption, $N_2$ activation, potential-determining step, and selectivity. As a result, a volcano plot of reactivity is established by using the valence electron number of $TM_1$ as the descriptor. Among all catalysts, $Cr_1$-$B_2N_2$/G exhibits superior performance with a limiting potential of -0.43 V with high selectivity of NRR interpreted by better spatial symmetry and excellent compatibility in terms of energy when $N_2$ interacts with $TM_1$. Our work reveals the general strategy of computational efforts to predict the next generation of advanced catalytic materials for NRR.

**Keywords:** Single-atom catalysts, ammonia synthesis, density functional theory, structure-activity relationship, descriptor

## INTRODUCTION

Ammonia ($NH_3$) is an extremely important chemical feedstock in human society and is widely used in the production of industrial chemicals such as fertilizers and pharmaceuticals[1]. The Haber-Bosch method converts hydrogen ($H_2$) and nitrogen ($N_2$) to $NH_3$ under high temperature (> 450 °C) and high pressure (> 100 atm), which consumes tremendous energy and releases plenty of $CO_2$[2-4]. In past decades, the electrocatalytic $N_2$ reduction reaction (NRR) has emerged as a promising technology for the production of $NH_3$ using $N_2$ and $H_2O$ as reactants at ambient conditions with much lower energy consumption[5-7]. However, the development of highly active and selective electrocatalysts for NRR remains a challenge due to the complexity of the reaction environment, which makes it difficult to accurately understand the correlation between activity and catalyst structure[8-13].

Single-atom catalysts (SACs) have exhibited outstanding specific activities for many electrochemical reactions[14-19]. Owing to high surface area and intriguing electrical properties, graphene-supported SACs have demonstrated excellent performance for NRR[20-22]. The well-defined structure in graphene-supported SACs offers great potential to modulate the active metal and corresponding coordination environment for establishing the structure-activity relationship and achieving high activity and selectivity[23-27]. The doping of B and N in the graphene structure has been reported to be beneficial for the adsorption and activation of reactants, thus enhancing the electrocatalytic activity of the catalyst. Due to the different electronegativity of B, N, and C, the interaction between active metal and substrate can be improved by electron transfer or charge rearrangement. Different B, N coordination environments can also modulate the chemical natures of active metal sites, giving rise to higher reactivity[28,29].

In this work, we investigated the NRR activity of all 3d transition metals in different $B_2N_2$ coordination environments by a high-throughput screening method. The comparative comparisons were performed in terms of stability, $N_2$ adsorption, $N_2$ activation, potential-determining step, and selectivity. Thus a volcano plot of reactivity was established by using the valence electron number of $TM_1$ as the descriptor, which can be understood that the chemical nature of the active center ($TM_1$ coordinated with B and N atoms) determines the electron donation process from $TM_1$ to $N_2$, which highly affect $N_2$ activation and subsequent hydrogenations. Moreover, the scenario demonstrated in this work offers guidance for the synthesis of efficient NRR catalysts by experiment.

### Computational details

All spin-polarization calculations were carried out by using the Vienna ab initio simulation package (VASP)[30,31]. The projector augmented wave (PAW) method was adopted to describe the ion-electron interactions[32]. The generalized gradient approximation in the Perdew-Burke-Ernzerhof (PBE) function was used[33,34], and the cut-off energy of 500 eV was set for the plane-wave basis. A 6 × 6 graphene supercell was used as the substrate with a 15 Å vacuum space and the Brillouin zone was sampled with the Monkhorst-Pack 3 × 3 × 1 and 7 × 7 × 1 k-point grids for geometry and electronic structure calculations, respectively. The cut-off energy, size of the graphene supercell, and the selection of k-points were referred to previous literature to ensure the accuracy of the calculation results [35-37]. The van der Waals (vdW) interactions between the adsorbates and catalysts are described by using Grimme's semiempirical DFT-D3 scheme[38]. The solvation effect was evaluated under an implicit solvent model VASPsol[39]. The energy and force convergence thresholds for the iteration in self-consistent field (SCF) were set to $10^{-5}$ eV and 0.02 eV·Å$^{-1}$, respectively. The calculation of COHP was done with the support of the Lobster program[40].

The adsorption energies ($E_{ads}$) of the NRR intermediates were obtained by the following equation:

$$E_{ads} = E_{total} - E_{clean\ catalysts} - E_{adsorbate} \quad (1)$$

In the above equation, the $E_{total}$, $E_{clean\ catalysts}$, and $E_{adsorbate}$ represent the total energies of the species-adsorbed catalysts system, clean catalysts, and adsorbate, respectively. According to this definition, the more negative adsorption energy indicates stronger adsorption of corresponding species.

The Gibbs free energy change ($\Delta G$) for each reaction step was calculated by the computational hydrogen electrode (CHE) model proposed by Nørskov and co-workers[41], which uses one-half of the chemical potential of hydrogen as the chemical potential of the proton-electron pairs. The $\Delta G$ was obtained by the following equation:

$$\Delta G = \Delta E + \Delta E_{ZPE} - T\Delta S + \Delta G_{pH} + eU \quad (2)$$

In the above equation, the $\Delta E$ is reaction energy obtained directly from the DFT calculation. The $\Delta E_{ZPE}$ and $T\Delta S$ are the contributions of the zero-point energy and entropy for the $\Delta G$. *T represents* the temperature, which is set as 298.15 K. The parameters $e$ and $U$ represent the number of electrons and the applied electrode potential, respectively. $\Delta G_{pH}$ is the free energy correction of pH, which can be determined as:

$$\Delta G_{pH} = k_B T \times pH \times \ln 10 \quad (3)$$

where the pH value was set to zero. The correction of the frequency was done with the support of the VASPKIT program[42]. In this work, the limiting potential ($U_L$) value was used as a descriptor of catalytic activity, which was determined by the potential-determining step (PDS) among six proton-coupled electron transfer (PCET) processes. $U_L$ was obtained by:

$$U_L = -\Delta G_{max}/e \quad (4)$$

Where $\Delta G_{max}$ represents the $\Delta G$ of the PDS.

## RESULTS AND DISCUSSION

### Structure and Stability of $TM_1$-$B_2N_2$/G

The 6 × 6 graphene supercell was first used as a substrate, four carbon atoms of which were replaced by two boron and two nitrogen atoms, giving rise to B/N doped graphene (denoted as $B_2N_2$/G). Then ten different 3*d* transition metal single atoms (denoted as $TM_1$) were selected and embedded as active centers (Sc, Ti, V, Cr, Mn, Fe, Co, Ni, Co, Zn) and coordinated with B or N via three different manners including two *cis*- and one *trans*- forms, distinguished as $TM_1$-$B_2N_2$/G-1 [Figure 1A], $TM_1$-$B_2N_2$/G-2 [Figure 1B], and $TM_1$-$B_2N_2$/G-3 [Figure 1C], respectively. Hence, a total of 30 different single-atom catalysts were constructed.

To assess the stability of the above $TM_1$-$B_2N_2$/G structures, we calculated the binding energies ($E_b$) of TM single atoms with substrates via equation (5) and the cohesion energy ($E_c$) by following equation (6) which refers to the energy of separating constituent metallic atoms apart from each other and assembling into the bulk:

$$E_b = E_{catalyst} - E_{TMsingle} - E_{support} \quad (5)$$

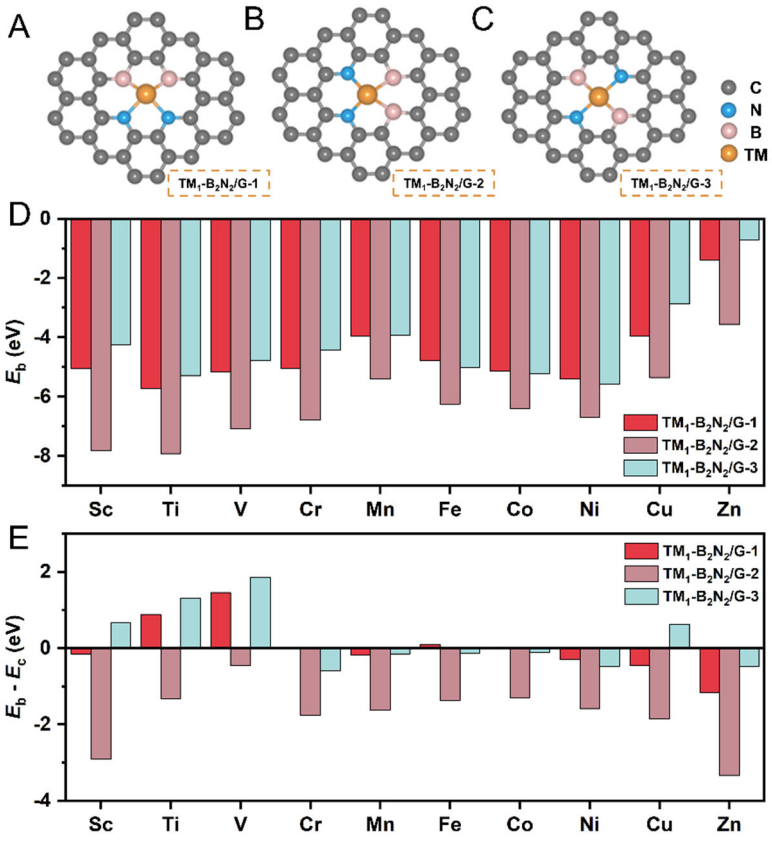


**Figure 1.** Structural stability of $TM_1$-$B_2N_2$/G catalysts. (A-C) The geometric structure of $TM_1$-$B_2N_2$/G catalysts; (D) The binding energy ($E_b$) of $TM_1$-$B_2N_2$/G catalysts; (E) The difference between binding energy and cohesion energy ($E_b$ - $E_c$) of $TM_1$-$B_2N_2$/G catalysts.

$$E_c = E_{TMbulk}/n - E_{TMsingle} \quad (6)$$

where $E_{TMbulk}$, $E_{TMsingle}$, and $n$ represent the energy of the bulk crystal cell of the transition metal, the energy of a single transition metal atom in the vacuum, and the number of atoms in the cell, respectively. Thereupon, we compared both the calculated $E_b$ and $E_b - E_c$ values in Figure 1D-E and Supplementary Table 1. The former metric indicates the binding strength of TM single atom with the support. For $TM_1$-$B_2N_2$/G catalysts, all $E_b < 0$ [Figure 1D], which means that all TM single atoms connect strongly with boron and nitrogen in graphene, and more negative values of $E_b$ underline that the *cis*-structures are more sturdy than *trans*-type. On the other side, $E_b$ - $E_c$ reflects the aggregation tendency of TM single atom, the more negative the values, the more stable the single atoms in the matrix of $B_2N_2$/G. Figure 1E exhibits that $E_b$ - $E_c < 0$ for most of $TM_1$-$B_2N_2$/G (except some Sc, Ti, V SACs), further demonstrating that the TM single atoms are anchored firmly rather than being subject to agglomeration. Additionally, the designing rationality of this work also could be verified by the fact that most of the structures above have been successfully synthesized by experiments and reported in the literature[43,44].

### Screen the NRR activities of $TM_1$-$B_2N_2$/G

After investigating the geometry and stability of the catalyst, we started to consider the adsorption and activation of $N_2$. According to previous studies, the high-performance NRR process requires: (1) $N_2$ spontaneously adsorbed on catalysts via chemical adsorption; (2) the free energy change of the first proton-coupled electron transfer (PCET) step should be appropriately low; (3) the limiting potential of the whole

process should be low enough throughout the NRR process; (4) the generated $NH_3$ on the catalyst surface can be easily desorbed after reaction; (5) the NRR process prevails while hydrogen evolution reaction (HER) is prohibited[45-47]. Hence, we followed the above hints to evaluate the NRR performance of $TM_1$-$B_2N_2$/G.

$N_2$ adsorption has a crucial influence on $N_2$ activation and the subsequent reaction process. After a careful summary of the literature, we considered two adsorption modes here: end-on and side-on configurations [Figure 2A][48]. The corresponding energies of $N_2$ adsorption are mapped in Figure 2B ($G_{ad}$) and Supplementary Table 2 ($E_{ad}$)-Supplementary Table 3($G_{ad}$). For most $TM_1$-$B_2N_2$/G catalysts, the negative or near zero values suggest $N_2$ can be spontaneously adsorbed on $TM_1$ [Supplementary Table 2 and Supplementary Table 3]. Meanwhile, the related N≡N lengths of adsorbed $*N_2$ showed significant increases (1.13~1.24 Å) compared to that of $N_2$ in vacuum (1.11 Å) [Supplementary Table 4], confirming that $N_2$ can be easily activated on these catalysts. In contrast, for $Cu_1$-$B_2N_2$/G and $Zn_1$-$B_2N_2$/G, both the relatively higher adsorption energies and negligible changes of N≡N lengths account for unsatisfactory $N_2$ activation on Cu or Zn single site; thus, $Cu_1$-$B_2N_2$/G and $Zn_1$-$B_2N_2$/G would not be considered in following sections.

The previous studies found that there were six PCET steps to accomplish the electrochemical reduction of $N_2$ and produced two $NH_3$ molecules[49-51]. Given that $N_2$ is a thermodynamic much stable molecule (dissociation energy of N≡N as 945 kJ·mol$^{-1}$), the first PCET plays a vital role among these steps because if the free energy change for this step is more positive, the following reaction would be more difficult to happen. Depending on $N_2$ adsorption behavior, the reaction proceeds through three pathways, as summarized in Supplementary Figure 1, i.e., the so-called distal or alternating mechanism (end-on) and enzymatic mechanism (side-on)[48]. When taking the former way, the first PCET step is $^*N_2 + H^+ + e^- \rightarrow {}^*NNH$, while in the enzymatic mechanism, the first PCET step is $^*N_2 + H^+ + e^- \rightarrow {}^*N\text{-}NH$. Taking all the possibilities into account, we calculated and summarized the free energy changes for this step in Figure 3A and Supplementary Table 5. Compared to other catalysts, the hotspots map illustrates that all $V_1$-$B_2N_2$/G and $Cr_1$-$B_2N_2$/G lay on red areas, suggesting both of the catalysts have lower energies for first PCET and $N_2$ adsorption with side-on pattern more energy-favorable than end-on. Among the three coordination environments of each $TM_1$, $V_1$-$B_2N_2$/G-1 and $Cr_1$-$B_2N_2$/G-1 had lower energies of the first PCET, 0.06 and 0.41 eV, respectively.

Subsequently, we simulated the whole NRR process for all $TM_1$-$B_2N_2$/G with three mechanisms, including 72 reaction paths and 576 steps, which were provided in Supplementary Figures 2-4. And 72 limiting potentials [$U_L$, Supplementary Table 6] of NRR can be sorted out and used as metrics to screen the activities or analyze the reaction mechanisms for all catalysts. Thus, the optimal activity and preferential reaction pathway for each catalyst are given in Figure 3B and C, with the $U_L$ values listed in Supplementary Table 7. The comparison of $U_L$ with the energies of the first PCET in Supplementary Figure 5 clearly demonstrates that the PDS of NRR on near 90 % $TM_1$-$B_2N_2$/G is the first PCET, which provides a convenient strategy for the preliminary screening of the catalysts. For all catalysts, the early transitional metal single atoms (e.g., Sc, V, Cr) generally have lower $U_L$ than late ones (e.g., Fe, Co, Ni) regardless of the coordination manners. Herein, $Cr_1$-$B_2N_2$/G SACs exhibit superior activities to other samples with $U_L$ as -0.43, -0.54, and -0.47 V for $Cr_1$-$B_2N_2$/G-1, $Cr_1$-$B_2N_2$/G-2, and $Cr_1$-$B_2N_2$/G-3, respectively. It is worth mentioning that although some $TM_1$-$B_2N_2$/G had lower first PCET energies (e.g., $Cr_1$-$B_2N_2$/G-1 with 0.41 eV, $V_1$-$B_2N_2$/G-1 with 0.59 eV), the $U_L$ values were uplifted due to more stable intermediates of $*NH\text{-}NH_2$ and *N, which were minority cases but had to be taken into account when using first PCET energy to guide catalyst designing. To get more insights into the catalytic mechanism, Figure 3C screens out the optimal NRR reaction pathways for all catalysts, and it is noted that the enzymatic mechanism triggered by side-on $N_2$ adsorption prevails compared to distal and alternating pathway, caused by modest adsorption energy for $N_2$ activation.

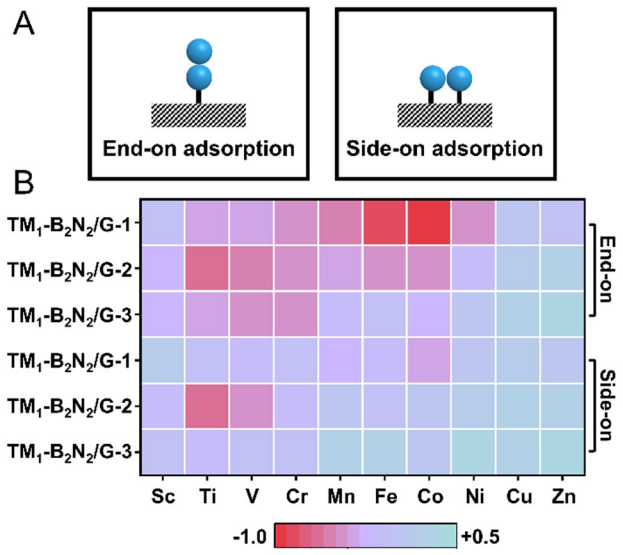


**Figure 2.** $N_2$ Adsorption. (A) Adsorption mode of $N_2$; (B) The heatmap of the free energy of adsorption of $*N_2$ ($G_{ad}$) for all $TM_1$-$B_2N_2$/G catalysts.

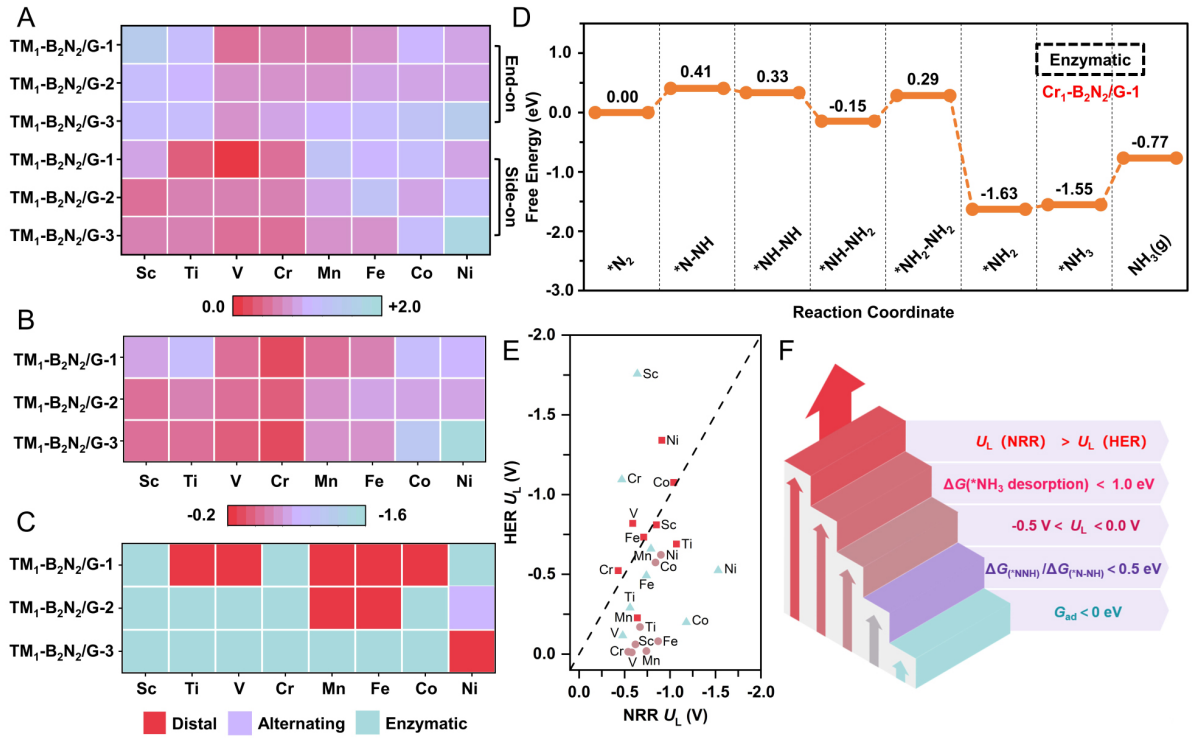


**Figure 3.** Catalytic studies of NRR. (A) Heatmap of the free energy change for the first PCET step; (B) Heatmap of the lowest NRR limiting potential ($U_L$) for all $TM_1$-$B_2N_2$/G catalysts; (C) Optimal reaction mechanism for all $TM_1$-$B_2N_2$/G catalysts; (D) Diagram of the NRR free energy change for the $Cr_1$-$B_2N_2$/G-1 catalyst; (E) Selectivity of NRR and HER for all $TM_1$-$B_2N_2$/G catalysts; (F) The proposed "five-step" strategy for high-throughput screening of NRR catalysts. NRR: $N_2$ reduction reaction.

However, when $N_2$ binds with the metal single atom strongly (e.g., Ti, V), the hydrogenation of *NH-NH in the enzymatic mechanism will become highly endothermic with an energy consumption of at least 1 eV,

then the reaction will prefer to follow the distal or altering pathway. When $N_2$ binds with metal single atom weakly (e.g. Fe, Co), the hydrogenation of the *NH-$NH_2$ intermediate will become highly endothermic, making the reaction will tend to follow the distal or alternate pathway. In particular, NRR processes catalyzed by more active $Cr_1$-$B_2N_2$/G catalysts are found to favorably take enzymatic way in Figure 3D and Supplementary Figure 6, which are triggered by first hydrogenations of $N_2$ with lower energies via side-on adsorption mode.

To complete the catalytic cycle, the derived $^*NH_3$ species need to be desorbed to restore the catalysts. The free energy changes of second $^*NH_3$ desorption (no PCET steps involved) are shown in Supplementary Figure 7. It can be seen that $^*NH_3$ desorption requires more energy input on the early transitional metals (e.g., Sc, Ti, V with 0.9~1.1 eV) than the late ones (e.g., Co, Ni with 0.5~0.7 eV). However, $Cr_1$-$B_2N_2$/G catalysts have moderate desorption energies to ensure easy desorption of $NH_3$ and lead to the higher reactivity of NRR [Figure 3B]. For instance, the energy on $Cr_1$-$B_2N_2$/G-1 is 0.78 eV, lower than $V_1$-$B_2N_2$/G-1 (0.95 eV). In addition, the protonation as $NH_4^+$ in the acidic electrolyte reaction conditions can further facilitate the $NH_3$ desorption[52,53].

From the above discussions, we can see that $Cr_1$-$B_2N_2$/G shows a superior activity towards NRR to other catalysts, and herein $Cr_1$-$B_2N_2$/G-1 performs the best, which are contributed by appropriate $N_2$ adsorption energy and adsorption mode that guarantee lower energy inputs requiring for $N_2$ activation, PDS (i.e., first PCET or the hydrogenation of $^*NH$-$NH_2$) and even the desorption of second $^*NH_3$.

The hydrogen evolution reaction is the key competing reaction during the NRR process. The presence of $^*H$ is facile to block TM single sites, which is deleterious for the NRR selectivity of the catalysts. To study the selectivity of catalysts, we compared the $U_L$ of the NRR and HER processes in Figure 3E. When $U_L$ (NRR) > $U_L$ (HER), i.e., the region above the dashed line, the electrochemical process is dominated by NRR. On the contrary, when $U_L$ (HER) > $U_L$ (NRR), i.e., the region below the dashed line, the electrochemical process is dominated by HER. According to this criterion, there are six $TM_1$-$B_2N_2$/G-1 or 3 (TM = Sc, V, Cr, Fe, Co, Ni) expected to exhibit higher selectivities of NRR over HER, including the most active $Cr_1$-$B_2N_2$/G-1.

### The descriptor for NRR activity of $TM_1$-$B_2N_2$/G

The high-throughput calculations of the $TM_1$-$B_2N_2$/G catalysts after a 5-step screening strategy [Figure 3F] allow to establish a volcano plot of the reaction activity [i.e, optimal $U_L$, Figure 4A] as the active centers of 3 *d* $TM_1$ varying from the left to right but with same coordination environments. $Cr_1$-$B_2N_2$/G catalysts exhibit better NRR activities regardless of the coordination of $Cr_1$. In order to guide the rational design of NRR catalysts with high performance, we chose the valence electron numbers of $TM_1$ in the catalysts as the descriptor δ that is highly associated with $N_2$ adsorption/activation and could be easily characterized by spectroscopy methods. Here δ is defined as the number of valence electrons of the transition metal. And it is the sum of the *d*-electron number of the transition metal and the Bader charge that the metal receives from the substrate. As shown in Figure 4B, a similar volcano relationship is constructed between NRR activities and δ for $TM_1$-$B_2N_2$/G. The effective catalysts for NRR can be found at δ = 4.5 to 6.0, e.g., $Cr_1$-$B_2N_2$/G. Although the estimation of δ descriptor by computation or readily characterization allows predicting the NRR catalysts with outstanding reactivity, the understanding of the above-disputed structure-activity connection remains unambiguous.

The above comprehensive comparisons in terms of $U_L$ and reaction pathways disclose that the NRR activity of $TM_1$-$B_2N_2$/G is determined by $N_2$ activation and hydrogenation of key intermediates (e.g., $^*NH$-NH or $^*NH$-$NH_2$), so-called PDS, which are apparently with respect to the interaction between $N_2$ and $TM_1$.

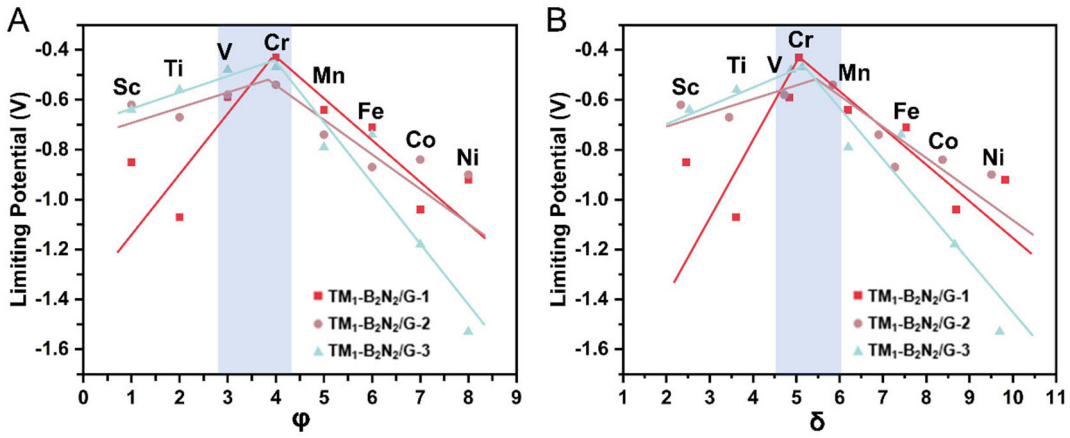


**Figure 4.** Descriptors of NRR activity. (A) Relationship between *d*-electron number of metal and NRR activity; (B) Relationship between valence electron number of metal in $TM_1$-$B_2N_2$/G and NRR activity. NRR: $N_2$ reduction reaction.

Additionally, it is believed that the electronic structure of metallic sites in $TM_1$-$B_2N_2$/G is of significant importance in investigating $N_2$ adsorption and activation. Therefore, we chose the most active $Cr_1$-$B_2N_2$/G as a probe to interpret the influence of $TM_1$ chemical nature and its corresponding steric coordination on the NRR activity.

### Understanding the charge transfer during $N_2$ activation

As shown in the electrostatic potential diagrams [Figure 5A-C] of three $Cr_1$-$B_2N_2$/G, isolated Cr sites have positive potentials (blue zone), while B sites show negative potentials (red zone) and N sites nearly remain electrically neutral (green zone), suggesting that when Cr doped in the lattice of $B_2N_2$/G, the charge transfer mainly occurred between Cr and B atoms rather than N atoms. Similar phenomena of electron migration can be seen from the charge density difference diagrams of $Cr_1$-$B_2N_2$/G [Supplementary Figure 8A-C]. The yellow region represents electron accumulation and the cyan region represents electron depletion. It is obvious that the charges are dominantly located at B sites and only a tiny amount of charges gather at N sites. Correspondingly, the electrons are accumulated at Cr sites. Therefore, the discrete charge distributions point that the interactions between Cr and B/N result in B atoms primarily donor electrons to Cr atoms as evidenced by the charge density distribution [Supplementary Figure 9].

Next, the partial density of states [PDOS, Figure 5D-F] reveals that the interactions between Cr and B/N atoms were achieved via the couplings of *d*(Cr)-*p*(B/N) orbitals. The interplay of *d*(Cr) with *p*(B) occurs throughout Fermi energy level ($E_F$), whereas the overlaps between *d*(Cr) and *p*(N) orbitals are only happened below $E_F$, proving that the Cr-B binding is more intensive than Cr-N, matching with the above analysis of charge transfer process. Continuously, the electron localization function (ELF) was applied to check the bonding characteristics of Cr with B/N; meanwhile, the electron distributions between B and N were also inspected to survey the influence of coordination (i.e., *cis* and *trans*) on the chemical nature of Cr. Here the ELF was illustrated by contour plots in real space with values from 0 to 1. The number 1 means the complete localization of electrons, implying covalent bonds may form between Cr and B/N, while 0 means complete delocalization of electrons, implying the formation of ionic bonds. In particular, 0.5, marked as a line, corresponds to the free electron gas, implying metallic bonds may form considering the semimetal properties of boron[54,55]. The calculated ELF values were summarized in Supplementary Table 8 and mapped in Figure 5G-I. It is noted that a similar ELF (Cr-N) of 0.74~0.78 are found for three $Cr_1$-$B_2N_2$/G, indicating

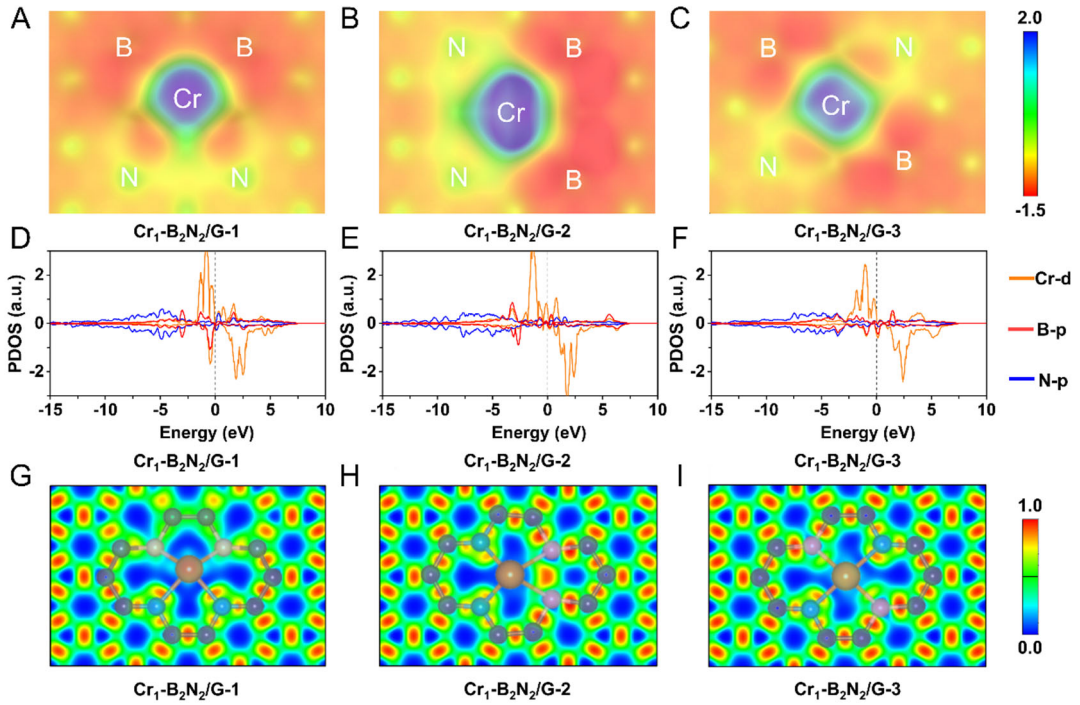


**Figure 5.** Electronic structure of $Cr_1$-$B_2N_2$/G catalysts. (A-C) The electrostatic potential (EP) of $Cr_1$-$B_2N_2$/G catalysts; (D-F) The partial density of states (PDOS) of $Cr_1$-$B_2N_2$/G catalysts; (G-I) The electron localization function (ELF) of $Cr_1$-$B_2N_2$/G catalysts.

the electrons are mainly delocalized in between instead of any elemental site. In contrast, the localization of electrons for Cr-B binding is different from each other catalyst, evidenced by three distinct ELF of 0.387, 0.308, 0.645 for $Cr_1$-$B_2N_2$/G-1, $Cr_1$-$B_2N_2$/G-2, and $Cr_1$-$B_2N_2$/G-3 respectively. Such a deviation can be interpreted by the electronic stereo interferences between B···B (or N) site affected by the distances, e.g., 2.90, 2.01, > 3.8 Å for B···B in three catalysts with ELF computed as 0.037, 0.814 and not available for *trans* sample [Supplementary Table 8], validating that the electron localization associated with the interplay of B···B (or N) follows the order of $Cr_1$-$B_2N_2$/G-2 > $Cr_1$-$B_2N_2$/G-3 > $Cr_1$-$B_2N_2$/G-1, whereas these electrons would not contribute to the charge transfer between Cr and B, resulting in the distinguished Bader charges of Cr as 1.156, 0.862 and 0.943 for three $Cr_1$-$B_2N_2$/G catalysts [Supplementary Table 9]. The higher charge densities are expected to deliver better performance of NRR activity for $Cr_1$-$B_2N_2$/G-1.

With the electronic structures of $Cr_1$-$B_2N_2$/G catalysts in mind, we continued to study the interaction of $N_2$ with the Cr single atom, which was of paramount importance for the following PCET processes and NRR activity. It was uncovered that the $N_2$ molecule preferential adsorbed on Cr with side-on mode [Figure 3]. The prolonged N≡N bond lengths of ~1.21Å (versus 1.11 Å in vacuum) verified the successful activation of $N_2$ rather than physical adsorption [Supplementary Table 2 and Supplementary Table 3]. Figure 6A-C visualizes the charge transfer in $N_2$ activation process on three $Cr_1$-$B_2N_2$/G, showing that the charge is migrated from Cr to N.

Subsequently, the orbital interactions related to $N_2$ activation were analyzed by PDOS [Figure 6D-F]. Generally, the interaction of $N_2$ with Cr was achieved by the $d$(Cr)-$\pi^*$($N_2$) orbital couplings. As illustrated in Figure 6B, the better spatial symmetry and the excellent compatibility in terms of energy for these two orbitals favors a stronger interaction between $N_2$ and $Cr_1$-$B_2N_2$/G-1 at 2.21 eV and 4.35 eV compared to the cases of $Cr_1$-$B_2N_2$/G-2 and $Cr_1$-$B_2N_2$/G-3, which may be contributed by the more charge densities of Cr in

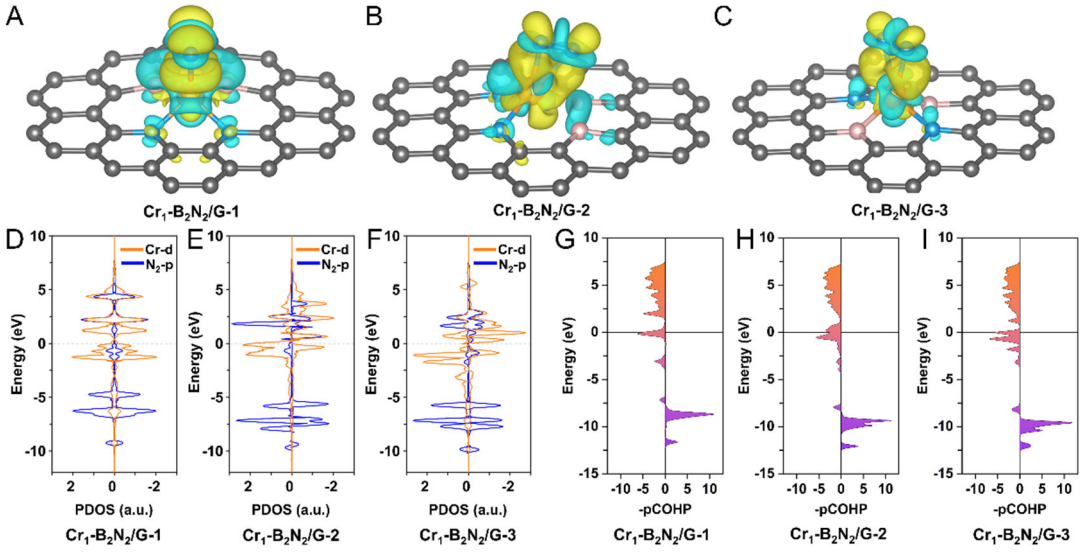


**Figure 6.** Investigation of the interaction between $N_2$ and $Cr_1$-$B_2N_2$/G. (A-C) The charge density difference of $N_2$ adsorbed on different $Cr_1$-$B_2N_2$/G catalysts. The isosurface value was set to be 0.002 e·Å$^{-3}$; (D-F) The PDOS of the *d*-orbitals of Cr and the *p*-orbitals of $N_2$ in the $Cr_1$-$B_2N_2$/G catalysts for $N_2$ adsorption; (G-I) The partial Crystal Orbital Hamiltonian Population (pCOHP) of N≡N bonds in $Cr_1$-$B_2N_2$/G catalysts adsorbed with $N_2$ in Side-on mode.

$Cr_1$-$B_2N_2$/G-1 [Supplementary Table 9]. The above stronger synergistic effect also effectively eliminates the spin polarization effect of the active site and ensures a higher NRR activity, as reported in the literature[56]. In addition, the intensive interplay of $N_2$ with $Cr_1$-$B_2N_2$/G-1 can also be proved by the energy level splitting of *d*(Cr) orbitals that originally dominated at 2.56 eV [Figure 5D].

To have a quantitative comparison of $N_2$ activation on three $Cr_1$-$B_2N_2$/G catalysts, the binding strength of N≡N bonds in the activated $N_2$ molecule was examined by the partial Crystal Orbital Hamiltonian Population (pCOHP)[57]. As depicted in Figure 6G-I, the bonding (-pCOHP > 0) and antibonding (-pCOHP < 0) contributions are shown on the right and left of one panel for each catalyst, respectively. The bonding contributions below the fermi level follow the order of $Cr_1$-$B_2N_2$/G-1 (-1.65) < $Cr_1$-$B_2N_2$/G-3 (-2.12) < $Cr_1$-$B_2N_2$/G-2 (-2.18), agreeing well with the integral COHP values, which are -1.24, -1.35, and -1.32, respectively. Here more negative ICOHP values indicate stronger N≡N bonds. On the contrary, the weaker binding strength of N≡N corresponds to a higher level of $N_2$ activation, as evidenced by the Bader charges of activated N≡N as 0.568, 0.413, 0.458 [Supplementary Table 10], which thus favors the subsequent hydrogenation reaction. This is consistent with the limiting potential order of $Cr_1$-$B_2N_2$/G-1 (-0.43 V) < $Cr_1$-$B_2N_2$/G-3 (-0.47 V) < $Cr_1$-$B_2N_2$/G-2 (-0.58 V) in Supplementary Table 7.

In this regard, the structure-activity relationship revealed for $Cr_1$-$B_2N_2$/G can be generalized to other transitional metals. That is to say, the NRR activities of $TM_1$-$B_2N_2$/G are mainly governed by the charge transfers between $N_2$ and metal atoms, i.e., more electrons lend from the metal to $N_2$, and higher NRR reactivity is obtained for the catalysts. Therefore, the descriptor of δ is further correlated with the Bader charge of activated N≡N [Supplementary Figures 10-15] for the most active catalyst in each group of $TM_1$-$B_2N_2$/G. Interestingly, a volcano trend of N≡N Bader charge depended on the valence electron number (δ) of the transitional metal single atom can be observed in Supplementary Figure 16. Such a connection reveals that the physical nature of $TM_1$ intrinsically dominates the interaction between $N_2$ and the active site, which determines $N_2$ activation and the subsequent consecutive hydrogenation, even the desorption of *

$NH_3$. The obtained knowledge paves the way for the development of advanced NRR.

## CONCLUSION

High-throughput DFT calculations were implemented to investigate the NRR performance of $TM_1$-$B_2N_2$/G, which was distinguished by different transitional metals and coordination configurations. Among all catalysts, $Cr_1$-$B_2N_2$/G-1, with better activity and selectivity, was found by a "five-step" screening strategy, which has an NRR limiting potential of -0.43 V. The volcano shape of the structure-activity relationship highlights the importance of the valence electron number of $TM_1$ as a descriptor, which can accelerate the rational design process of advanced NRR catalysts. In addition, it was revealed that the limiting potentials were highly relevant with electron donation from $TM_1$ to $N_2$, which determined the $N_2$ activation and potential-determining step. The scenario demonstrated in this work offers guidance for the synthesis of efficient NRR catalysts by experiment.

## DECLARATIONS

### Authors' contributions

Conceptualization, calculation, data curation, data analysis, and original draft: Cao N
Calculation, data organization, and data analysis: Zhang N
Data analysis: Wang K
Resources: Yan K
Conceptualization, resources, data analysis, review and writing: Xie P

### Availability of data and materials

The data that support the findings of this study are available from the corresponding author upon reasonable request.

### Financial support and sponsorship

This work was supported by the National Natural Science Foundation of China (22278365), the National Key Research and Development Program of China (2022YFE0128600), the Natural Science Foundation of Zhejiang Province (LR22B060002), and a grant from Shanxi-Zheda Institute of Advanced Materials and Chemical Engineering (2021ST-AT-002).

### Conflicts of interest

All authors declared that there are no conflicts of interest.

### Ethical approval and consent to participate

Not applicable.

### Consent for publication

Not applicable.



## REFERENCES

1. Comer BM, Fuentes P, Dimkpa CO, et al. Prospects and challenges for solar fertilizers. *Joule* 2019;3:1578-605. DOI
2. Smil V. Detonator of the population explosion. *Nature* 1999;400:415-415. DOI
3. Licht S, Cui B, Wang B, Li FF, Lau J, Liu S. Ammonia synthesis. Ammonia synthesis by $N_2$ and steam electrolysis in molten hydroxide suspensions of nanoscale $Fe_2O_3$. *Science* 2014;345:637-40. DOI PubMed

4. Qian J, An Q, Fortunelli A, Nielsen RJ, Goddard WA 3rd. Reaction mechanism and kinetics for ammonia synthesis on the Fe(111) surface. *J Am Chem Soc* 2018;140:6288-97. DOI
5. Guo W, Zhang K, Liang Z, Zou R, Xu Q. Electrochemical nitrogen fixation and utilization: theories, advanced catalyst materials and system design. *Chem Soc Rev* 2019;48:5658-716. DOI
6. Suryanto BHR, Du H, Wang D, Chen J, Simonov AN, Macfarlane DR. Challenges and prospects in the catalysis of electroreduction of nitrogen to ammonia. *Nat Catal* 2019;2:290-6. DOI
7. Niu L, Wang D, Xu K, et al. Tuning the performance of nitrogen reduction reaction by balancing the reactivity of $N_2$ and the desorption of $NH_3$. *Nano Res* 2021;14:4093-9. DOI
8. Pang Y, Su C, Jia G, Xu L, Shao Z. Emerging two-dimensional nanomaterials for electrochemical nitrogen reduction. *Chem Soc Rev* 2021;50:12744-87. DOI PubMed
9. Yang Z, Wang J, Wang J, et al. 2D $WO_{3-x}$ nanosheet with rich oxygen vacancies for efficient visible-light-driven photocatalytic nitrogen fixation. *Langmuir* 2022;38:1178-87. DOI PubMed
10. Giuffredi G, Asset T, Liu Y, Atanassov P, Di Fonzo F. Transition metal chalcogenides as a versatile and tunable platform for catalytic $CO_2$ and $N_2$ electroreduction. *ACS Mater Au* 2021;1:6-36. DOI PubMed PMC
11. Wu T, Melander MM, Honkala K. Coadsorption of NRR and HER intermediates determines the performance of Ru-$N_4$ toward electrocatalytic $N_2$ reduction. *ACS Catal* 2022;12:2505-12. DOI
12. Majumder M, Saini H, Dědek I, et al. Rational design of graphene derivatives for electrochemical reduction of nitrogen to ammonia. *ACS Nano* 2021;15:17275-98. DOI
13. Lee CH, Pahari S, Sitapure N, Barteau MA, Kwon JS. DFT–kMC analysis for identifying novel bimetallic electrocatalysts for enhanced NRR Performance by suppressing her at ambient conditions via active-site separation. *ACS Catal* 2022;12:15609-17. DOI
14. Wang Y, Su H, He Y, et al. Advanced electrocatalysts with single-metal-atom active sites. *Chem Rev* 2020;120:12217-314. DOI
15. Li X, Liu L, Ren X, Gao J, Huang Y, Liu B. Microenvironment modulation of single-atom catalysts and their roles in electrochemical energy conversion. *Sci Adv* 2020:6. DOI PubMed PMC
16. Li L, Chang X, Lin X, Zhao ZJ, Gong J. Theoretical insights into single-atom catalysts. *Chem Soc Rev* 2020;49:8156-78. DOI
17. Hu S, Tian N, Li M, et al. Trapezohedral platinum nanocrystals with high-index facets for high-performance hydrazine electrooxidation. *Chem Synth* 2023;3:4. DOI
18. Kaiser SK, Chen Z, Faust Akl D, Mitchell S, Pérez-Ramírez J. Single-atom catalysts across the periodic table. *Chem Rev* 2020;120:11703-809. DOI PubMed
19. Kim J, Choi S, Cho J, Kim SY, Jang HW. Toward multicomponent single-atom catalysis for efficient electrochemical energy conversion. *ACS Mater Au* 2022;2:1-20. DOI PubMed PMC
20. Novoselov KS, Geim AK, Morozov SV, et al. Electric field effect in atomically thin carbon films. *Science* 2004;306:666-9. DOI
21. Stoller MD, Park S, Zhu Y, An J, Ruoff RS. Graphene-based ultracapacitors. *Nano Lett* 2008;8:3498-502. DOI PubMed
22. Tan C, Cao X, Wu XJ, et al. Recent advances in ultrathin two-dimensional nanomaterials. *Chem Rev* 2017;117:6225-331. DOI
23. Zhuo HY, Zhang X, Liang JX, Yu Q, Xiao H, Li J. Theoretical understandings of graphene-based metal single-atom catalysts: stability and catalytic performance. *Chem Rev* 2020;120:12315-41. DOI
24. Liu P, Nørskov JK. Ligand and ensemble effects in adsorption on alloy surfaces. *Phys Chem Chem Phys* 2001;3:3814-8. DOI PubMed
25. Li X, Shen P, Luo Y, et al. PdFe single-atom alloy metallene for $N_2$ electroreduction. *Angew Chem Int Ed Engl* 2022;61:e202205923. DOI PubMed
26. Ren G, Shi M, Liu S, Li Z, Zhang Z, Meng X. Molecular-level insight into photocatalytic reduction of $N_2$ over Ruthenium single atom modified $TiO_2$ by electronic Metal-support interaction. *J Chem Eng* 2023;454:140158. DOI
27. Zhang A, Liang YX, Zhang H, Geng ZG, Zeng J. Doping regulation in transition metal compounds for electrocatalysis. *Chem Soc Rev* 2021; 50:9817-9844. DOI
28. Vineesh TV, Kumar MP, Takahashi C, et al. Bifunctional electrocatalytic activity of boron-doped graphene derived from boron carbide. *Adv Energy Mater* 2015;5:1500658. DOI
29. Yu X, Han P, Wei Z, et al. Boron-doped graphene for electrocatalytic $N_2$ reduction. *Joule* 2018;2:1610-22. DOI
30. Kresse G, Furthmüller J. Efficiency of ab-initio total energy calculations for metals and semiconductors using a plane-wave basis set. *Comput Mater Sci* 1996;6:15-50. DOI
31. Kresse G, Furthmüller J. Efficient iterative schemes for ab initio total-energy calculations using a plane-wave basis set. *Phys Rev B Condens Matter* 1996;54:11169-86. DOI PubMed
32. Blöchl PE. Projector augmented-wave method. *Phys Rev B Condens Matter* 1994;50:17953-79. DOI PubMed
33. Perdew JP, Chevary JA, Vosko SH, et al. Atoms, molecules, solids, and surfaces: Applications of the generalized gradient approximation for exchange and correlation. *Phys Rev B Condens Matter* 1992;46:6671-87. DOI
34. Perdew JP, Wang Y. Accurate and simple analytic representation of the electron-gas correlation energy. *Phys Rev B Condens Matter* 1992;45:13244-9. DOI PubMed
35. Yang WJ, Ren JN, Zhang HW, et al. Single-atom iron as a promising low-temperature catalyst for selective catalytic reduction of $NO_x$ with $NH_3$: a theoretical prediction. *Fuel* 2021;302:121041. DOI
36. Yang W, Zhao M, Ding X, et al. The effect of coordination environment on the kinetic and thermodynamic stability of single-atom iron catalysts. *Phys Chem Chem Phys* 2020;22:3983-9. DOI

37. Yang W, Xu S, Ma K, et al. Geometric structures, electronic characteristics, stabilities, catalytic activities, and descriptors of graphene-based single-atom catalysts. *NMS* 2020;2:120-31. DOI
38. Grimme S, Antony J, Ehrlich S, Krieg H. A consistent and accurate ab initio parametrization of density functional dispersion correction (DFT-D) for the 94 elements H-Pu. *J Chem Phys* 2010;132:154104. DOI PubMed
39. Gray CM, Saravanan K, Wang G, Keith JA. Quantifying solvation energies at solid/liquid interfaces using continuum solvation methods. *Mol Simul* 2017;43:420-7. DOI
40. Nelson R, Ertural C, George J, Deringer VL, Hautier G, Dronskowski R. LOBSTER: Local orbital projections, atomic charges, and chemical-bonding analysis from projector-augmented-wave-based density-functional theory. *J Comput Chem* 2020;41:1931-40. DOI PubMed
41. Nørskov JK, Bligaard T, Logadottir A, et al. Trends in the exchange current for hydrogen evolution. *J Electrochem Soc* 2005;152:J23. DOI
42. Wang V, Xu N, Liu J, Tang G, Geng W. VASPKIT: A user-friendly interface facilitating high-throughput computing and analysis using VASP code. *Comput Phys Commun* 2021;267:108033. DOI
43. Shi L, Bi S, Qi Y, et al. Anchoring mo single-atom sites on B/N codoped porous carbon nanotubes for electrochemical reduction of $N_2$ to $NH_3$. *ACS Catal* 2022;12:7655-63. DOI
44. Fan M, Chen X, Zhang M, Cui L, He X, Zou X. Highly dispersed Ru nanoclusters anchored on B,N co-doped carbon nanotubes for water splitting. *Inorg Chem Front* 2022;9:968-76. DOI
45. Niu H, Wang X, Shao C, Zhang Z, Guo Y. Computational screening single-atom catalysts supported on g-CN for $N_2$ reduction: high activity and selectivity. *ACS Sustainable Chem Eng* 2020;8:13749-58. DOI
46. Choi C, Back S, Kim N, Lim J, Kim Y, Jung Y. Suppression of hydrogen evolution reaction in electrochemical $N_2$ reduction using single-atom catalysts: a computational guideline. *ACS Catal* 2018;8:7517-25. DOI
47. Lv X, Wei W, Huang B, Dai Y, Frauenheim T. High-throughput screening of synergistic transition metal dual-atom catalysts for efficient nitrogen fixation. *Nano Lett* 2021;21:1871-8. DOI
48. Shi L, Yin Y, Wang S, Sun H. Rational catalyst design for $N_2$ reduction under ambient conditions: strategies toward enhanced conversion efficiency. *ACS Catal* 2020;10:6870-99. DOI
49. Jiao D, Liu Y, Cai Q, Zhao J. Coordination tunes the activity and selectivity of the nitrogen reduction reaction on single-atom iron catalysts: a computational study. *J Mater Chem A* 2021;9:1240-51. DOI
50. Liu S, Cheng Z, Liu Y, et al. Boosting electrochemical nitrogen reduction reaction performance of two-dimensional Mo porphyrin monolayers *via* turning the coordination environment. *Phys Chem Chem Phys* 2021;23:4178-86. DOI
51. Jin H, Guo C, Liu X, et al. Emerging two-dimensional nanomaterials for electrocatalysis. *Chem Rev* 2018;118:6337-408. DOI
52. Katsounaros I, Figueiredo MC, Chen X, Calle-vallejo F, Koper MTM. Structure- and coverage-sensitive mechanism of NO reduction on platinum electrodes. *ACS Catal* 2017;7:4660-7. DOI
53. Chun H, Apaja V, Clayborne A, Honkala K, Greeley J. Atomistic insights into nitrogen-cycle electrochemistry: a combined DFT and kinetic monte carlo analysis of NO electrochemical reduction on Pt(100). *ACS Catal* 2017;7:3869-82. DOI
54. Ma F, Jiao Y, Gao G, et al. Graphene-like two-dimensional ionic boron with double dirac cones at ambient condition. *Nano Lett* 2016;16:3022-8. DOI
55. Zhang H, Li Y, Hou J, Tu K, Chen Z. FeB6 Monolayers: The graphene-like material with hypercoordinate transition metal. *J Am Chem Soc* 2016;138:5644-51. DOI PubMed
56. Sun X, Zhang H, Wang S, et al. Tuning the coordination microenvironment to boost the electrocatalytic HER activity of $M_3(C_6O_3S_3)_2$. *J Phys Chem C* 2022;126:16606-14. DOI
57. Deringer VL, Tchougréeff AL, Dronskowski R. Crystal orbital Hamilton population (COHP) analysis as projected from plane-wave basis sets. *J Phys Chem A* 2011;115:5461-6. DOI PubMed